Causality in the shock wave/turbulent boundary layer interaction

Kenzo Sasaki [ORCID],[1] Diogo C. Barros [ORCID],[2] André V. G. Cavalieri [ORCID],[1] and Lionel Larchevêque [ORCID][2]

[1]*Instituto Tecnológico de Aeronáutica (ITA), Aerodynamics Department, São José dos Campos, 12228900 Brazil*

[2]*Aix Marseille Université, CNRS, IUSTI, Marseille, 13453 France*

In shock wave/boundary layer interactions, two mechanisms have been recognized to drive the low-frequency unsteadiness of the reflected shock: upstream boundary layer forcing and downstream feedback. The current work presents a quantitative analysis of the causal mechanisms underlying such flow unsteadiness. The analysis is based on a large-eddy simulation database covering approximately 300 cycles of the low-frequency shock fluctuations in a Mach 2 turbulent boundary layer. This time span enables the accurate application of frequency-domain system identification methods targeting such low frequencies. The evaluation of the spectrum in the interaction zone indicates that the broadband low-frequency unsteadiness is predominantly two-dimensional and can be isolated via spanwise averaging. Empirically derived transfer functions are computed using the averaged flow field and indicate the occurrence of a feedback between the locations downstream of the flow separation and the shock fluctuations. The results indicate that this mechanism dominates over the upstream forcing of the interaction region. Accordingly, the computed transfer functions are also used as an estimation tool to predict the shock motion accurately; for the largest streamwise separation between input and output signals, correlations above 0.6 are observed between predictions and raw data. Computation of spectral proper orthogonal decomposition modes reveals the existence of upstream traveling waves in the leading spectral mode at the main shock frequency; higher frequencies do not exhibit this trend. Furthermore, the spectral modes obtained using selected flow regions downstream of the shock enable the reconstruction of a significant portion of the energy in the interaction zone. Finally, a linear stability analysis is conducted using the mean turbulent flow, showing the existence of upstream traveling waves. Evaluation of a vortex sheet model indicates that these upstream traveling modes are of acoustic nature. The predicted modes from this local analysis present a compelling match against the spectral modes, both in terms of the shape and phase speed of the fluctuations. The combined analysis of the techniques indicates that downstream disturbances are the dominant cause of shock oscillations in the present configuration, leading to shock motion by upstream traveling acoustic modes.

I. INTRODUCTION

Interactions between shock waves and turbulent flows appear in multiple high-speed applications including supersonic flight and combustion processes [1]. Specifically, in shock wave/boundary layer interactions (SBLI), the imposed adverse pressure gradient over the wall induces flow separation, which is associated with a reflected shock presenting highly unsteady low-frequency fluctuations. This situation occurs in many practical configurations such as turbomachinery flows, transonic buffeting, overexpanded rocket nozzles, and supersonic inlet isolators. Besides affecting

the flow downstream of the interaction zone, these oscillations are responsible for large pressure levels and severe structural loading. The source of these broadband shock fluctuations has been the subject of extensive debate and comprehensive reviews over the past decades [2–7].

Two mechanisms are recognized to induce reflected shock unsteadiness: upstream boundary layer forcing and downstream feedback [3]. Among numerous investigations [8–10], a strong correlation between the upstream boundary layer streamwise velocity and shock motion was found in the experiments of Ganapathisubramani *et al.* [11]. Three-dimensional measurements from Humble *et al.* [12] demonstrated that low- and high-momentum streamwise-elongated zones convected within the incoming boundary layer affect directly the reflected shock structure. On the other hand, there is compelling evidence for the influence of the downstream separated flow on the shock motion. The large-eddy simulations (LES) and linear stability analysis of Touber and Sandham [13] suggested the existence of unstable modes and upstream traveling waves associated with a global instability mechanism is responsible for the low-frequency shock oscillations. These oscillations were found to be highly correlated to the reattachment pressure measurements performed by Dupont *et al.* [14]. The direct numerical simulation (DNS) of Wu and Martin [15] also pointed to a strong correlation where the shock motion lags behind the reattachment fluctuations. The mass-entrainment model proposed by Piponniau *et al.* [16] scales the low-frequency content with the separated flow region and highlights the importance of the downstream flow on selecting the shock unsteadiness. It is worth noting that a low-frequency feedback from the reattachment region up to the vicinity of the reflected shock was documented for transitional SBLI [17,18]. Although the flow features listed above could suggest that a similar mechanism may also be at play for turbulent SBLI, this seems not to have been demonstrated in the current literature.

The low-frequency unsteadiness and the associated mechanisms discussed above were observed for impinging oblique shocks and compression ramp configurations, in both numerical and experimental investigations. Equally important is the spatial organization of the low-frequency motion in the vicinity of the reflected shock and separation bubble. The low-pass filtered velocity fields from the simulations of Priebe and Martín [19] highlighted a strong quasi-two-dimensional behavior of the reflected shock motion using spanwise averaging. The dynamic mode decomposition analysis (DMD) conducted by Priebe *et al.* [20] shows that the shock unsteadiness was reproduced using a number of low-frequency DMD modes. Their spatial imprint qualitatively agreed with the linear unstable modes found by Touber and Sandham [13]. These modes exhibit streamwise-elongated structures in the downstream separation bubble of the compression ramp. Similar streamwise Görtler-like vortices were found in the DMD analysis from Pasquariello *et al.* [21] for a strong impinging shock wave. The global stability analysis and dynamic modes computed over spanwise-averaged velocity fields by Nichols *et al.* [22] shows a striking resemblance with the recirculation bubble breathing during one cycle of the oscillation.

All mechanisms described above exist in the SBLI interaction. It is unclear, however, to what extent each mechanism causes the low-frequency unsteadiness. Here, we present a causal analysis to determine the influence of both the upstream and downstream flow on the unsteady shock behavior. We exploit the LES database from Jiang *et al.* [23], where an impinging shock wave interacts with a turbulent boundary layer at Mach number $\mathrm{Ma}_\infty = 2$ and $\mathrm{Re}_\theta \simeq 5000$. This database spans a time domain an order of magnitude larger than the current existing DNS or LES simulations investigated for this configuration [13,21,24], corresponding roughly to more than 300 low-frequency cycles. This time span allows the application of system identification methods targeting specifically the reflected shock frequency. First, we conduct a linear transfer function analysis to identify the link between the shock motion and flow locations. This provides a quantitative evaluation of causality. The analysis also accounts for a time-domain prediction determining how much of the shock fluctuations can be recovered from single measurements. The technique, used in turbulent jets [25] and boundary layers [26], leads to a linear estimator between an input and an output. Here, if the shock fluctuations are taken as an output, consideration of inputs given by flow fluctuations at various positions allows an assessment of a causal link to shock motion. If such a link exists,

TABLE I. Flow parameters.

Ma$_\infty$	p_o	T_o	U_∞	δ_{99}	Re$_\theta$	L	W
2	40 500 Pa	295 K	510 ms^{-1}	11 mm	4850	57 mm	33 mm

a causal convolution of the input with the obtained transfer function should lead to an accurate reconstruction of low-frequency shock fluctuations.

To clarify the spatial structure of the low-frequency unsteadiness, we perform a spectral proper orthogonal decomposition (SPOD) of the spanwise-averaged velocity fields in the interaction zone [27,28]. Since it is derived in the frequency domain, SPOD is computed at the specific shock frequency, isolating its motion. From these modes, an empirically calculated frequency wave-number spectrum is also obtained, which highlights the occurrence of upstream traveling fluctuations. Application of SPOD in subdomains, such as upstream or downstream regions, may be used to evaluate how much spatial structures in these specific locations are coherent with shock motion. Such an approach is thus complementary to the linear transfer functions, providing spatial modes related to shock fluctuations. Moreover, SPOD modes are known to be related to optimal response modes obtained from resolvent analysis [28,29]. If nonlinearities in the Navier-Stokes system are modeled as white noise, SPOD modes become equivalent to the most amplified flow responses in a linearized input-output formulation. Hence, it is appropriate to compare SPOD modes to modes obtained with the linearized Navier-Stokes operator; although an exact correspondence is not expected, since nonlinear terms are colored [30,31], dominant amplification mechanisms may lead to clear similarities between SPOD and resolvent modes. Moreover, the analysis of the linearized response provides the mechanisms that underpin the coherent motion. Here, the analysis of the linearized operator will be carried out in a simplified manner, with a local stability analysis conducted at stations with significant amplitudes of the leading SPOD mode. We anticipate that a spatially growing, upstream traveling mode is obtained, thus providing a physical mechanism explaining the influence of the recirculation region on the shock oscillations. The remainder of the paper is organized as follows. In Sec. II, a description of the numerical database is provided, accounting for the whole set of simulation and flow parameters. The key spectral features of the shock motion are analyzed in Sec. III. The mathematical framework to compute the linear transfer functions, causal analysis, and spectral decomposition is presented in Sec. IV. We report the prediction and causality results in Sec. V, the spectral eigenvalues and modes in Sec. VI, and the linear stability analysis in Sec. VII. Finally, the concluding remarks are presented in Sec. VIII.

II. NUMERICAL DATABASE

The current large-eddy simulation (LES) reproduces the shock wave/turbulent boundary layer interaction investigated in the experiments of Schreyer *et al.* [32]. The full description of the numerical simulation was presented by Jiang *et al.* [23], together with a thorough validation against wind-tunnel measurements. Here, we provide a brief overview of the configuration and main flow parameters.

The numerical setup mimics the experimental shock generated by a flow deflection of 8.5° impinging on a Ma$_\infty = 2$ turbulent boundary layer with Re$_\theta \simeq 5000$. The complete set of flow parameters is listed in Table I. The incident shock corresponds to a pressure ratio of 1.58 with an angle of approximately 38°, as indicated in Fig. 1. All simulations were performed using the FLU3M codes from ONERA, Office National d'Etudes et de Recherches Aérospatiales. The code relies on a finite volume discretization in space and an implicit time integration, both being second-order accurate. The space scheme is designed to minimize the numerical dissipation by adding the dissipative part of the Roe scheme to a centered scheme in regions with strong compressibility/low vorticity, as identified by means of Ducros's sensor [33,34]. The time integration is performed
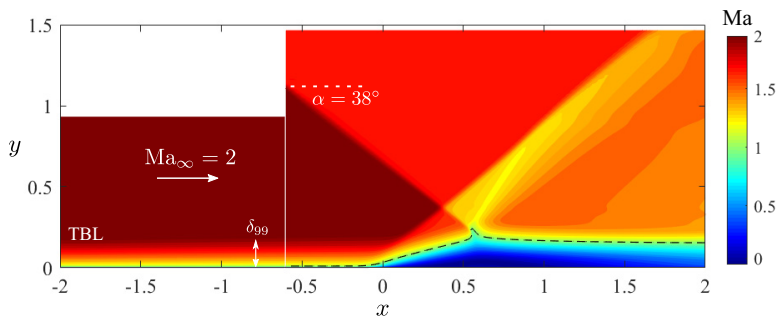
FIG. 1. Mean Mach number in the streamwise (x) wall-normal (y) longitudinal plane at $z = 0$. The turbulent boundary layer (TBL) thickness (δ_{99}) is shown in the first region of the simulation, and the sonic line is represented in the interaction zone.

with a maximum Courant–Friedrichs–Lewy number of 11, using seven subiterations to solve the nonlinear system in order to ensure that residuals are reduced by at least 1.5 orders of magnitude. The LES modeling is built from an implicit grid filtering coupled with an explicit subgrid modeling through the selective mixed-scale model that was successfully used in previous studies of shock wave/boundary layer interactions [35,36].

The wall is modeled as adiabatic. Nonreflective boundary conditions relying on characteristic variation in space are set at the inflow, outflow, and upper boundaries, while periodicity is used in the spanwise z direction. The incident shock is created by enforcing the pre- and postshock states on the upper boundaries, following Garnier *et al.* [36]. A fully turbulent inflow condition is obtained by adding stochastic velocity fluctuations to the mean profiles by means of a synthetic eddy method (SEM) [37]. Temperature and density fluctuations are obtained from the velocity fluctuations assuming strong Reynolds analogy and linearized ideal gas law with negligible pressure fluctuations [38]. The space and timescales required by SEM are obtained from a pre-existing LES of the same $Ma_\infty = 2$ boundary layer without shock impingement that encompasses the laminar-to-turbulent transition process [39]. Comparisons between the two LES demonstrate that a relaxing length of about 10 boundary layer thicknesses δ_{99} is sufficient to achieve fully turbulent canonical first- and second-order statistics from the inflow boundary condition.

The reference mesh was designed by setting the inflow location $16\delta_{99}$ upstream of the shock impingement location. The grid resolution and spanwise extent W of the computational domain were increased with respect to previous studies [35]. The corresponding resolution in wall units were $\Delta x^+ = 28$ (streamwise), $\Delta y^+_{\min} = 0.85$ (wall-normal), and $\Delta z^+ = 12$ (spanwise) for $W = 3\delta_{99}$. Two additional meshes were tested for a grid-convergence study: a refined one with resolution increased by 40%, 20%, and 30% in the streamwise, wall-normal, and spanwise directions, respectively, and an enlarged spanwise domain corresponding to $W = 6\delta_{99}$.

A key characteristic of the numerical database is that data is sampled from the reference mesh over approximately 300 periods of the typical low-frequency unsteadiness, as will be discussed later. It allows the computation of statistical and spectral quantities, and even conditional statistics with a very low level of statistical uncertainty. Computations from the two additional meshes were performed for 10 to 18 low-frequency cycles. These tests were long enough to achieve statistical convergence for validation purposes.

A complete description with validation results from the experimental database and grid convergence can be found in Jiang *et al.* [23]. All the computations and experiments have an interaction length of $L = 5.2\delta_{99}$ and the mean velocity profiles upstream of and within the interaction region agree very well. Downstream of the interaction region, the LES velocity fields relax toward a canonical boundary layer profile slightly more slowly than in the experiments. This was explained by the finite width of the experimental setup with side walls compared to the periodicity set in the computations.
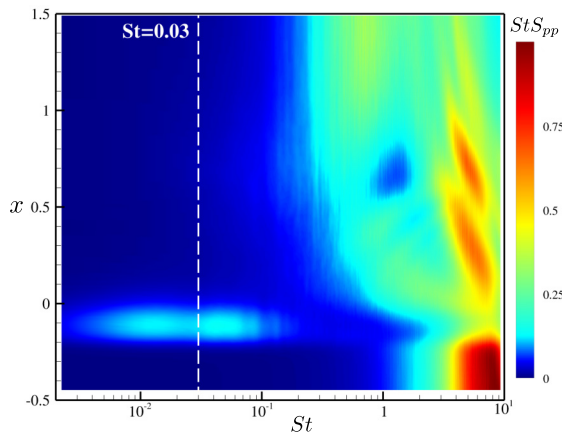
FIG. 2. Streamwise evolution of the premultiplied and normalized spectrum of the wall pressure fluctuations p ($z = 0$).

Second-order velocity statistics also show very good agreement between the three computations and the particle image velocimetry measurements, with the exception of the streamwise fluctuations in the incoming boundary layer and the initial stage of the mixing layer developing over the separated region. In the latter, the LES underestimate the $\overline{u'u'}$ level by 40% whatever the mesh used. Comparisons between the streamwise velocity spectra obtained from the LES and the experiments show that the underestimation originates solely in the low-frequency band $f\,\delta_{99}/U_\infty < 0.15$. This difference is assigned to the intrinsic inability of the present SEM method in generating large-scale convective structures found in experiments [11]. These structures possibly originate in the nozzle upstream of the flat surface or follow from a long development of the boundary layer, and neither of them were simulated in the numerical setup. Although the impact of such discrepancies is not fully understood, these are not expected to affect our resulting conclusions, given the otherwise good agreement between LES and experiments for the spectral quantities of interest in multiple locations over the wall.

III. SPECTRAL ANALYSIS OF THE SHOCK MOTION

A space-time spectral analysis is considered to identify the key features of the shock motion. The variables are normalized by the interaction length scale L and the free-stream velocity U_∞. The dimensionless time is defined as $t = t^* U_\infty / L$, while the normalized frequency reads St $= fL/U_\infty$, corresponding to the Strouhal number.

First, we assess the dominant frequency in the vicinity of the shock. The streamwise evolution of the premultiplied spectrum of pressure fluctuations is shown in Fig. 2. The spectrum is defined as $S_{pp} = \langle \hat{p}\hat{p}^* \rangle$, where $\hat{}$ indicates the Fourier transform from time to frequency f and $\langle . \rangle$ defines an ensemble averaging. In the upstream boundary layer ($x < -0.25$), the spectrum presents mainly high-frequency content (St > 1) linked to the incoming turbulent eddies. However, in the vicinity of the shock position ($-0.2 < x < 0$), a low-frequency broadband range emerges, and it is centered approximately at St $= 0.03$. The large gap between these frequency scales was reported in previous investigations [14,40]. As discussed later in the paper, a low-pass filter will be applied to the data to isolate these shock oscillations.

To shed further light on the spatial structure of these oscillations, the frequency wave-number diagrams are computed for the streamwise velocity fluctuations. Here, $S_{uu}(\text{St}, \beta) = \langle \hat{\hat{u}}\hat{\hat{u}}^* \rangle$, where the double hat indicates a double Fourier transform, from time to f and from z to the spanwise normalized wavenumber β. Figure 3 presents the two-dimensional spectra in the near-wall region
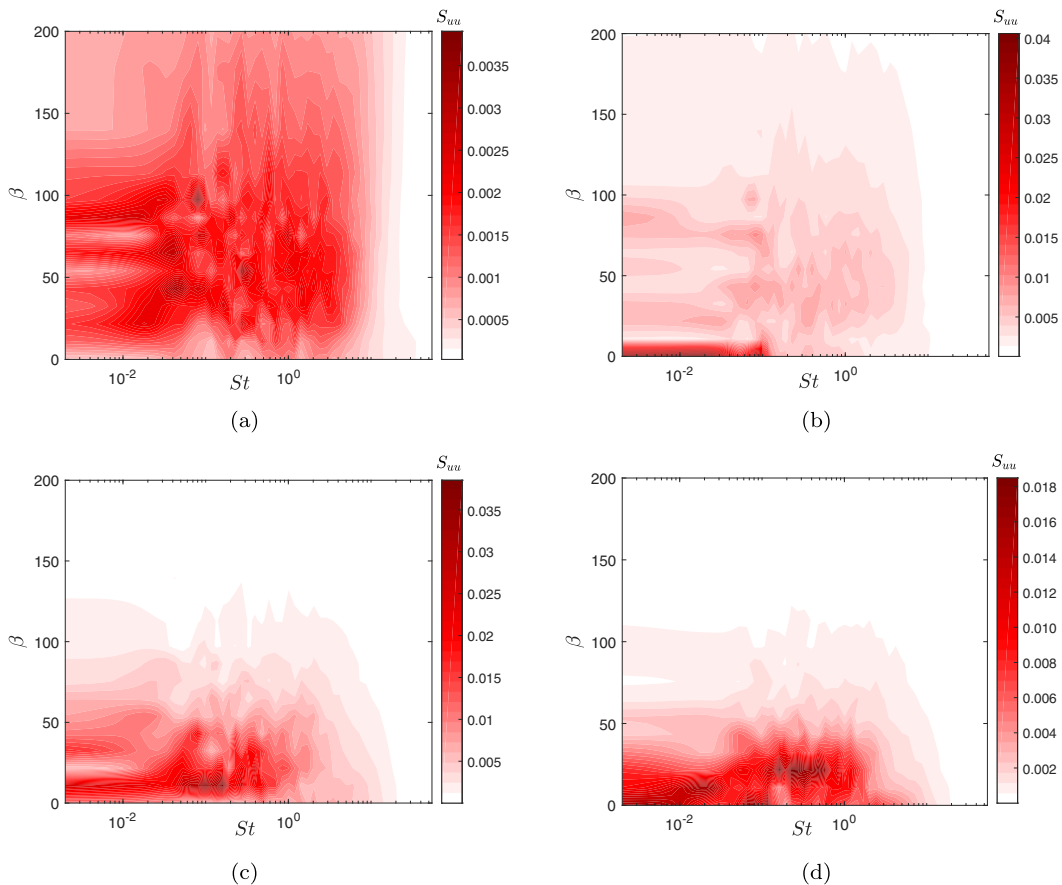
FIG. 3. Two-dimensional spectra at $x = -0.35, 0.0, 0.2$, and 1.4, respectively in panels (a) to (d).

at four streamwise locations $x = -0.35$, 0.0, 0.2, and 1.4. These locations correspond to the upstream boundary layer, the approximate shock position, the recirculating bubble, and downstream reattachment, respectively. Upstream of the shock, the flow is dominated by broadband turbulent near-wall streaks. In the approximate shock position, the fluctuations are quasi-two-dimensional ($\beta = 0$). As discussed above, this region is predominantly governed by low-frequency fluctuations, which can therefore be isolated via spanwise averaging. This property will be considered and analyzed in our flow predictions. The values of β increase in the recirculating flow region and further downstream. The velocity fluctuations exhibit mostly a three-dimensional behavior, and the characteristic frequencies are also higher in this region. The simultaneous increase of both St and β are related to the development of shear-layer vortices and their breakup into 3D eddies. This could be linked to the existence of Görtler-type structures developing along the boundary layer, as observed in previous investigations [24,41].

IV. METHODS

A. Linear transfer function: single-input single-output analysis

A linear, frequency-domain system identification method is applied to relate an input signal $I(t)$ to an output $O(t)$ separated in the streamwise/wall-normal plane. The supporting assumption for the method is the existence of a linear function that maps the input to the output locations.

A similar approach was applied to estimate velocity fluctuations in turbulent jets and boundary layers [25,26]. Our goal is to identify the causal mechanisms behind the low-frequency shock unsteadiness. The problem is formulated in the frequency domain, where an estimator may be defined by minimizing, in a least squares sense, the coherence between the error of the estimation and the input measurement. The resulting frequency response [42,43] reads

$$G_{IO}(f) = \frac{S_{IO}(f)}{S_{II}(f)}, \tag{1}$$

where $S_{II}(f)$ and $S_{IO}(f)$ are the auto and cross spectra of the input and output signals, respectively, and $G_{IO}(f)$ refers to the empirical transfer function computed in the frequency domain [42]. These quantities were calculated from the expected values of $\hat{I}(f)\hat{I}^*(f)$ and $\hat{I}(f)\hat{O}^*(f)$, obtained from an ensemble averaging, via Welch's method. The spectra were obtained using 230 blocks of 2000 elements, each with an overlap of 75%, which results in a frequency resolution of 0.015. Similar results were obtained using up to 5000 elements in each block.

Equation (1) is referred to as the H_1 estimator of the system, and it minimizes the error due to measurement noise in the output [43]. Other formulations, such as the H_2 or H_v estimators, exhibit different performances in terms of sensor noise minimization. However, they are expected to perform equally well for this type of estimation, which does not consider the presence of measurement uncertainties and is based in simulation data. The H_1 estimator presents the interesting property of leading to a prediction error which is linearly uncorrelated with the input [43,44], therefore resulting in the best linear prediction of the output signal.

Once the transfer function $G_{IO}(f)$ is computed, its time-domain counterpart is recovered by means of an inverse Fourier transform:

$$g_{IO}(t) = \int_{-\infty}^{+\infty} G_{IO}(f)e^{-i2\pi ft}df. \tag{2}$$

The function $g_{IO}(t)$ represents a linear convolution kernel, and therefore allows one to estimate the output via the convolution with the input signal

$$O(t) = \int_{-\infty}^{\infty} g_{IO}(\tau)I(t-\tau)d\tau. \tag{3}$$

The dummy variable τ was introduced for the calculation of the convolution.

B. Hillbert transform to evaluate causality

The convolution in Eq. (3) is taken between $\pm\infty$. However, for a causal prediction, this operation should be limited from 0 to $+\infty$, so that only past information is used to predict the output signal. The convolution operation is usually limited to the causal part of the convolution kernel, which permits an online prediction of the output. This type of approach is necessary for active closed-loop applications, for example. Nevertheless, the full convolution operation may also be used for data reconstruction, a feature which was explored in Ref. [26] for a turbulent boundary layer.

This implies that if $g_{IO}(t < 0) \neq 0$, there is some reverse causality between input and output signals. An evaluation of the convolution kernel in the time domain can therefore be used to determine the causality relation between input and output positions. Such evaluations in the time domain could be cumbersome and, in some cases, qualitative, particularly for positions which are close to each other, where a feedback path usually occurs. To avoid this problem, the evaluation of causality can be performed directly in the frequency domain by means of the Hilbert transform [45]. This method has the advantage of testing several locations in a fast, computationally efficient manner. The Hilbert transform is a linear operation that performs a convolution with the function $1/(\pi f)$,

$$H(F(f)) = \frac{1}{\pi} \int_{-\infty}^{+\infty} \frac{F(\Omega)}{f-\Omega} d\Omega. \tag{4}$$

Hilbert transforms are commonly used in signal processing for the design of causal filters, and the idea was adopted in flow control applications to determine suitable positions for the active control of shear layers [46]. A causal filter results when $g_{IO}(t \leqslant 0) = 0$. This occurs in convectively unstable flows, such as Tollmien-Schlichting or Kelvin-Helmholtz dominated shear flows, where upstream measurements are taken to estimate downstream fluctuations. Computation of the Hilbert transform, in this case, is made directly in the frequency domain by means of a convolution with the previously calculated empirical transfer function.

The approach consists in exploring the following property of the transform: If the imaginary part of the frequency response (interpreted here as a transfer function) of a linear system is equal to the Hilbert transform of the real part, the system represents a causal, linear filter. Hence, knowledge of the real part is sufficient to completely specify the system, with the imaginary part adding redundant information [42].

Therefore, a quantitative evaluation of the causality of the transfer function $G_{IO}(f)$ may be obtained by computing the correlation between its imaginary part and the Hilbert transform of its real part. This parameter is given by

$$P = \frac{\int_{-\infty}^{\infty} H(\text{Re}[G_{IO}(f)])\text{Im}[G_{IO}(f)]df}{\sqrt{\int_{-\infty}^{\infty} H(\text{Re}[G_{IO}(f)])^2 df}\sqrt{\int_{-\infty}^{\infty} \text{Im}[G_{IO}(f)]^2 df}}. \tag{5}$$

Values of P close to unity indicate a causal behavior between input and output positions, with a reverse causality occurring as P approaches zero. This parameter will be used in the following section to evaluate the causality between two different locations.

C. Spectral proper orthogonal decomposition

To characterize the spatial features of the coherent motion at a given frequency, spectral proper orthogonal decomposition is applied in the streamwise/wall-normal plane. As outlined in Sec. III, the low-frequency shock dynamics can be considered mostly two-dimensional. Therefore, spanwise averaging of the 14 streamwise/wall-normal planes available from the LES data set is considered to isolate the $\beta = 0$ fluctuations. The effect of the spanwise averaging on the signal prediction framework discussed above is reported in Sec. V (Fig. 4).

The objective is to extract spatially coherent fluctuations for a given frequency, in particular the low-frequency shock oscillations and its relation to the recirculating flow region. The SPOD is used here as an auxiliary tool to observe the causes of the shock unsteadiness and to visualize the propagation of the fluctuations for a targeted frequency within the SBLI. SPOD was employed in a number of studies [27,28,47–49].

The spectral decomposition is applied to the spanwise-averaged streamwise/wall-normal (u, v) velocity fluctuations such that they are optimal modes to represent the turbulent kinetic energy. The modes are defined from the solution of the following integral equation:

$$\int_{\Omega} \mathbf{\Gamma}(\mathbf{x}, \mathbf{x}', f)\mathbf{W}(\mathbf{x}')\psi_j(\mathbf{x}', f)d\mathbf{x}' = \lambda\psi_i(\mathbf{x}, f). \tag{6}$$

Here, $\mathbf{x} = (x, y)$, Ω is the spatial domain where the flow is defined and $\mathbf{W}$ is a weight of appropriate dimension. ψ_i corresponds to an eigenfunction (*i*th SPOD mode) with corresponding eigenvalue λ and $\mathbf{\Gamma}(\mathbf{x}, \mathbf{x}', f)$ is the two-point cross spectral density, which is defined from the Fourier transform of the correlation tensor

$$\mathbf{\Gamma}(\mathbf{x}, \mathbf{x}', f) = \int_{-\infty}^{\infty} \mathbf{C}(\mathbf{x}, \mathbf{x}', \tau)e^{i2\pi f\tau}d\tau. \tag{7}$$
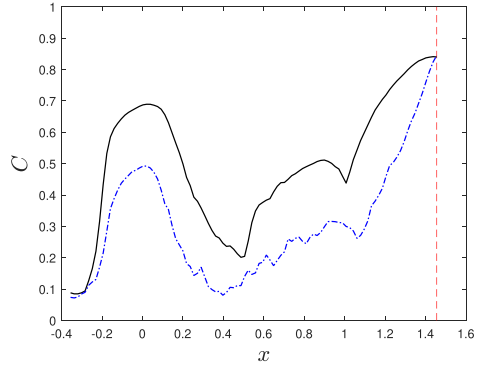
The correlation tensor $\mathbf{C}$ is obtained by

$$\mathbf{C}(\mathbf{x}, \mathbf{x}', \tau) = E[\mathbf{q}(\mathbf{x}, t)\mathbf{q}^*(\mathbf{x}', t + \tau)], \tag{8}$$
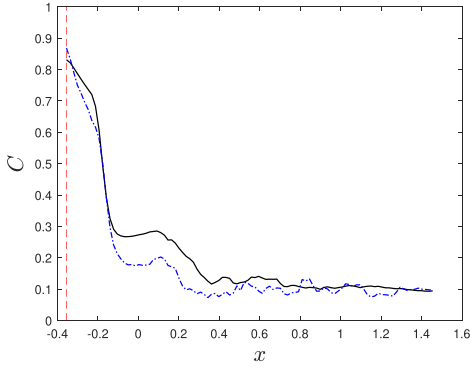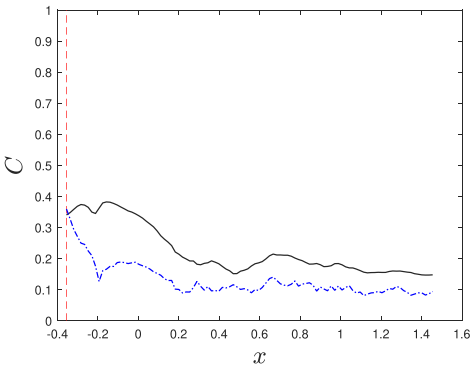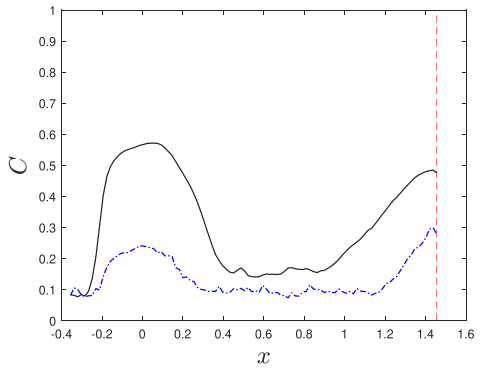
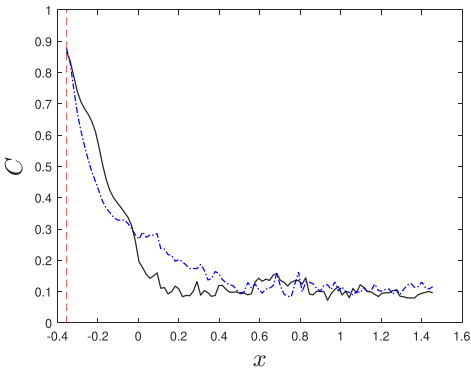(a)Input upstream of the shock, pressure/pressure estimation

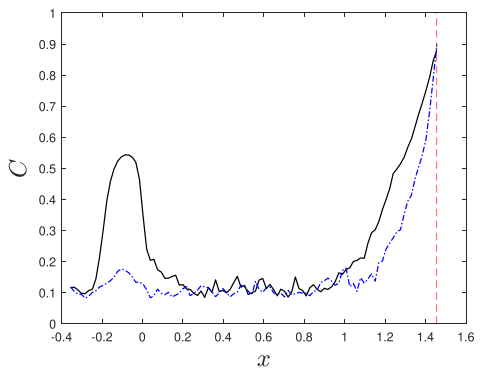(b)Input downstream of the shock, pressure/pressure estimation

(c)Input upstream of the shock, velocity/pressure estimation

(d)Input downstream of the shock, velocity/pressure estimation

(e)Input upstream of the shock, velocity/velocity estimation

(f)Input downstream of the shock,velocity/velocity estimation

FIG. 4. Correlation between prediction and LES for pressure and streamwise velocity components. The vertical dashed line presents the position of the input. Solid black lines correspond to the prediction performed with the spanwise averaging and dash-dotted blue lines correspond to that without it.

with $\mathbf{q} = (u, v)$ being the velocity components, $*$ representing the conjugate transpose, and $E[.]$ supplying an expectation operator consisting of an ensemble time average, representing the expected value of a given realization of the flow field.

In this work, the method of snapshots is considered to compute the SPOD modes. The continuous two-point cross spectral density [Eq. (7)] is replaced by an inner product,

$$\mathbf{\Gamma}_{ij} = \langle \hat{\mathbf{q}}_i, \hat{\mathbf{q}}_j \rangle. \tag{9}$$

where $\hat{\mathbf{q}}_\mathbf{i} = [\mathbf{u}_i, \mathbf{v}_i]^T$, with the superscript T representing a transpose, denotes the ith realisation of the velocity field (i.e., the ith short-time Fourier transform of the snapshot of the velocity field). Such formulation is motivated by the use of Welch's method in the computation of the cross-spectral densities.

By using the snapshot method of Eq. (9), the infinite-dimensional integral eigenvalue problem in (6) is reduced to an $N \times N$ matrix eigenvalue problem for every frequency f_k, where N is the number of blocks in Welch's method. The eigenvalue problem can be shown to reduce to [28]

$$\mathbf{\Gamma}_{f_k} \psi_{f_k} = \psi_{f_k} \lambda_{f_k}. \tag{10}$$

The SPOD modes of the discrete problem can be constructed from the columns of ψ_{f_k}. For further details regarding the snapshots method and the transformation of the integral equation to a matrix eigenvalue problem, the reader is referred to the paper by Towne *et al.* [28] and the Appendix of Sasaki *et al.* [48].

The elements in Eq. (9) were determined by means of the Welch's method, with a triangular window and 75% overlap of the segments. Each segment has 5000 points with a time discretization of $\Delta t = 0.026$. The total number of elements in the time signal considered is to be 342 900, which results in 97 blocks for averaging. These parameters were observed to be adequate to resolve the flow structures in the particularly low frequencies of interest. Different windows were also considered and led to similar results.

V. TRANSFER FUNCTIONS IN THE INTERACTION ZONE

A. Prediction performance

We start by assessing the accuracy of the single-input single-output linear transfer functions in predicting the velocity and pressure fluctuations in the averaged shock position. As introduced in Fig. 2, the shock unsteadiness presents a frequency one order of magnitude lower than the turbulent fluctuations. Therefore, in order to isolate the shock motion, the fluctuations were low-pass filtered using a finite-impulse-response (FIR) filter with a cutoff frequency of St = 0.3 to avoid the influence of higher frequency flow structures. The filter is applied prior to the calculation of the transfer functions. A window size consisting of 2000 points, which corresponds to $\Delta t = 60$ with an overlap of 75%, was used in the Welch's method for calculation of the power spectra. Similar results were also obtained for window sizes consisting of 5000 points. To avoid spurious values of the transfer function, frequencies where $S_{IO}(f)$ is below a certain threshold are set to zero. This occurs for frequencies higher than the cutoff filter.

Three input/output pairs were computed: pressure/pressure, velocity/pressure, and velocity/velocity. Here, only the causal part of the convolution kernel was considered to compute the prediction; i.e., g_{IO} was forced to zero when $t < 0$. To quantitatively evaluate the prediction performance, the normalized correlation between the estimation $O_{\text{est}}(t)$ and the LES data $O_{\text{LES}}(t)$ was computed,

$$C = \frac{\int_{-\infty}^{\infty} O_{\text{LES}}(t) O_{\text{est}}(t) dt}{\sqrt{\int_{-\infty}^{\infty} O_{\text{LES}}^2(t) dt} \sqrt{\int_{-\infty}^{\infty} O_{\text{est}}^2(t) dt}}, \tag{11}$$

where O_{LES} and O_{est} are the LES and the estimated data, respectively. The normalized correlation in the previous equation varies between zero and one, where one indicates a perfect correlation between predicted and LES signals.

Two input positions were considered separately, upstream and downstream of the shock. The correlation was computed as a function of the output (prediction) streamwise position. Figure 4

shows the resulting correlation between prediction and LES data, and the vertical line highlights the input location. The prediction was performed with and without the spanwise averaging of the input/output quantities.

As expected, the correlations decay as the distance between input and output positions increases; for the cases where the same variable is used as the measurement and prediction, the correlations depart from large values close to unity. When the input is upstream of the shock in Figs. 4(a), 4(c) and 4(e), the correlation decays monotonically up to the mean shock location $x = 0$ and stabilizes further downstream. On the other hand, in the case of an input downstream of the shock wave shown in Figs. 4(b), 4(d) and 4(f), the correlation also decays as the output position is moved further away from the input. However, close to the shock location, there is a swift increase in the correlation values. It should also be observed that even though there is a large separation between input and output, the correlation between prediction and input reaches values above 0.6.

The effect of the spanwise averaging is remarkable, leading to a significant increase in the correlation of the predicted signals, in particular when the input position is taken downstream of the shock motion. This is in accordance with the spectra of Fig. 3, which indicates a predominantly two-dimensional nature of the streamwise velocity shock-related fluctuations. Hereafter, only spanwise averaged data is considered.

Figure 5 presents a sample of the predicted streamwise velocity and pressure fluctuations at $x = 0$ with input at $x_{in} = 1.5$. It is noticeable that, even though the amplitude of the LES signal is underestimated, both the phase and the low-frequency content of the signal (characteristic of the shock motion) are well captured by this approach, in spite of the large streamwise separation between input and output. The damped fluctuations are associated with the limited linear transfer function estimation, as reported by Sasaki *et al.* [25]. Since the estimation error is linearly uncorrelated with the input, the damping is assumed to be linked to nonlinear mechanisms. The corresponding shape of the transfer function is depicted in Fig. 6.

### B. Wall-normal behavior and causality of the transfer function predictions

To further investigate the prediction performance and to track the causal areas for the shock fluctuations, the output position was fixed at $x = 0$, near the wall. Transfer functions were computed considering a grid of positions along the streamwise and wall-normal directions as input signals. As indicated above, we consider the spanwise averaged velocity fields low-pass filtered with the cutoff frequency $St = 0.3$ prior to the computation of the transfer functions. The same window size and overlap of the previous analysis were used for calculating the power spectra. The pressure fluctuation was considered as the estimated variable, with the streamwise velocity fluctuations as the input. Finally, the full convolution kernel including its noncausal counterpart was used here to evaluate signal reconstruction.

Figure 7(a) presents the resulting correlations between the shock prediction and LES data for the different inputs considered. High correlations appear in the near-shock region. This is expected due to the coherent shock motion; such high correlations are due to an input related to shock oscillations predicting the fluctuations at the shock foot. An interesting behavior occurs downstream of the shock ($x > 1.0$), where correlations of the order of 0.8 start to occur, indicating that these can be used to accurately estimate the shock motion. In the region $0.2 < x < 1.0$, within the recirculation bubble, the correlations drop to low values, a feature which can be assessed by the shape of the SPOD modes presented in following section.

In order to determine the causal effects of the shock, Figs. 7(b) and 7(c) present two indices, the P parameter, related to the causality between input and output positions, and the group velocity. The latter can be estimated from the time delay observed in the empirically calculated transfer function and the streamwise separation between input and output positions. As an example, consider the time-domain transfer function computed using the streamwise velocity fluctuation at the positions of $x_{in} = 1.5$ and $x_{out} = 0$, shown in Fig. 6. The streamwise separation is of -1.5, with a time delay for the peak of the transfer function corresponding to approximately $\Delta t = 2$, which results in an
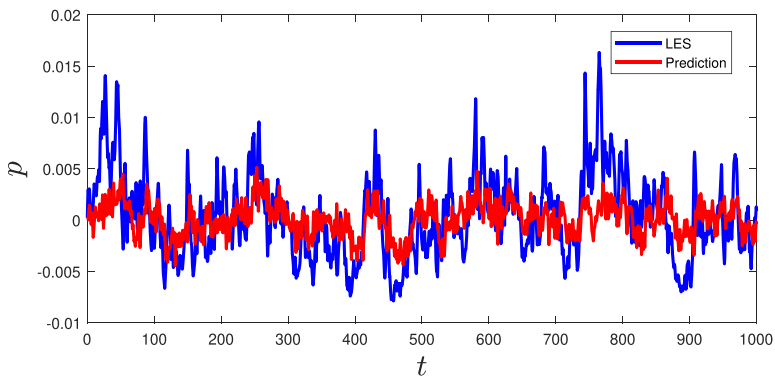
(a)Input downstream of the shock, pressure/pressure estimation
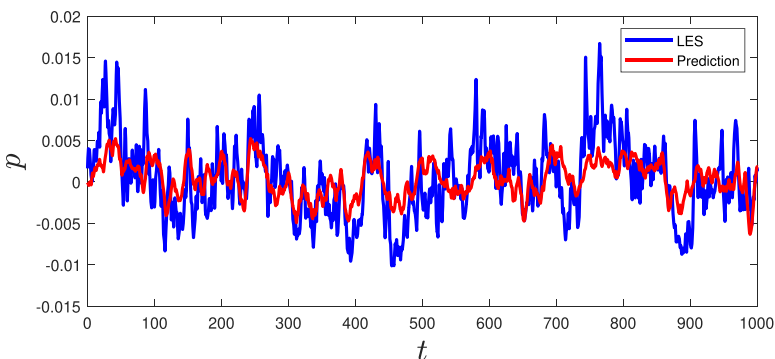
(b)Input downstream of the shock, velocity/pressure estimation
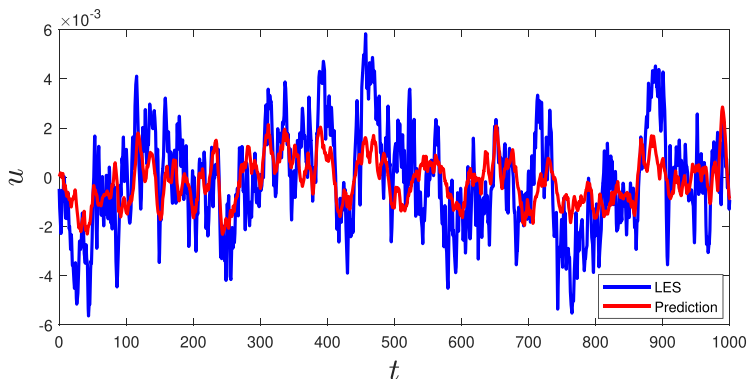
(c)Input downstream of the shock, velocity/velocity estimation

FIG. 5. Comparison between the time signals from LES and linear prediction, for pressure (a) and stream-wise velocity (b) fluctuations. The predicted position corresponds to $x = 0$ (average position of the shock) and the input is located at $x = 1.5$ downstream of the shock.

estimated group velocity of $v_g = -0.75$, normalized with respect to the free-stream velocity U_∞. As the bulk of the transfer function is for positive time delays, the causality parameter P is calculated as 0.9, indicating a nearly causal behavior. Regions where the the P parameter was between 0.3 and 0.7, or where the correlation C between estimation and prediction was below 0.3, were not
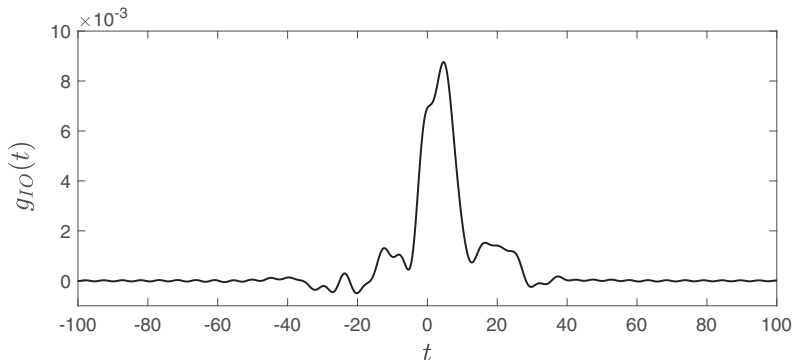
FIG. 6. Transfer function of the streamwise velocity fluctuations computed at the positions of $x_{in} = 1.5$ and $x_{out} = 0$.

considered in the computation of the group velocity and the value was set to $v_g = 0$. This avoids a nonphysical interpretation of this parameter near the $v_g = 0$ line or where the transfer function estimation is inaccurate.

When both the correlation C and P parameter in Figs. 7(a) and 7(b) are analyzed together, we note that the only causal input locations (large P) that lead to high correlations with shock motion (large C) surrounds the recirculation bubble and extends downstream of it. In particular, the parameter P and the group velocity indicate causality between shock oscillations at $x = 0$ from fluctuations near the reattachment point and downstream of the recirculation bubble. The computed negative group velocity points to fluctuations that are propagating upstream from the input location. In addition, the high correlation values indicate that fluctuations at downstream locations precede shock oscillations and enable an accurate prediction of its motion. Fluctuations occurring upstream of the shock present a positive group velocity and are not strongly correlated with its motion. These results are in agreement with previous observations from Touber and Sandham [13], who observed a negative phase speed in a similar configuration and related it to the existence of a global mode. The observations from Dupont *et al.* [14] and Wu and Martin [15] also point to a strong correlation between low-frequency fluctuations and the reattachment region. It is of interest to remark the existence of a region upstream of the shock with positive group velocity and large values of P. This region contributes to causing the shock motion, which is in accordance with the experiments from Ganapathisubramani *et al.* [50]. However, due to the relatively low correlation levels presented in Fig. 4(a), this region has a relatively lower contribution to the shock unsteadiness than the downstream zone in our numerical data without the presence of superstructures in the boundary layer. According to Figs. 4(a), 4(c) and 4(e), the upstream input locations are unable to accurately predict downstream fluctuations, where the correlations rapidly decay in the streamwise direction. Hence, upstream fluctuations do not have a significant role related to the larger scale separating and reattaching flow unsteadiness.

VI. UPSTREAM TRAVELING WAVES IN THE FLOW

A. Shape and velocity of the SPOD modes

In order to better understand the spatial structure of the low-frequency oscillations, SPOD modes of the spanwise averaged (u, v) velocity components were computed at St = 0.03 and St = 0.3. The first Strouhal number corresponds to the low-frequency motion and is representative of shock oscillations, whereas the second one is related to high-frequency boundary-layer and shear-layer fluctuations mostly uncorrelated to the shock. Figure 8 depicts the resulting eigenvalues for these two selected frequencies. The eigenvalues were ranked in descending order. In both cases, there is
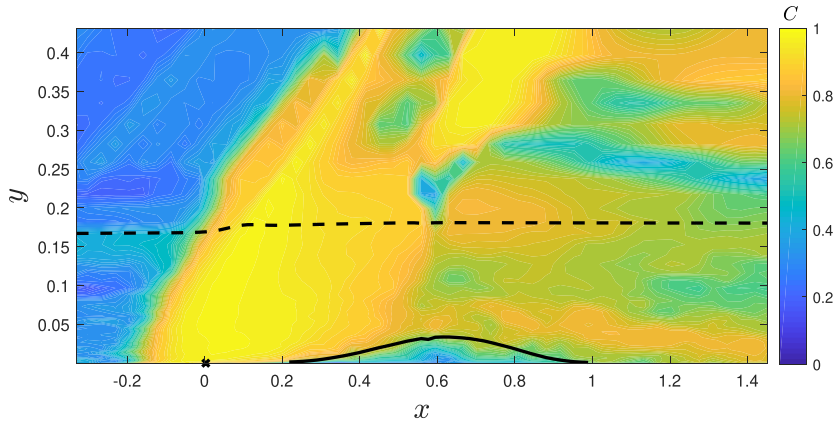
(a)Correlations between estimated and LES data
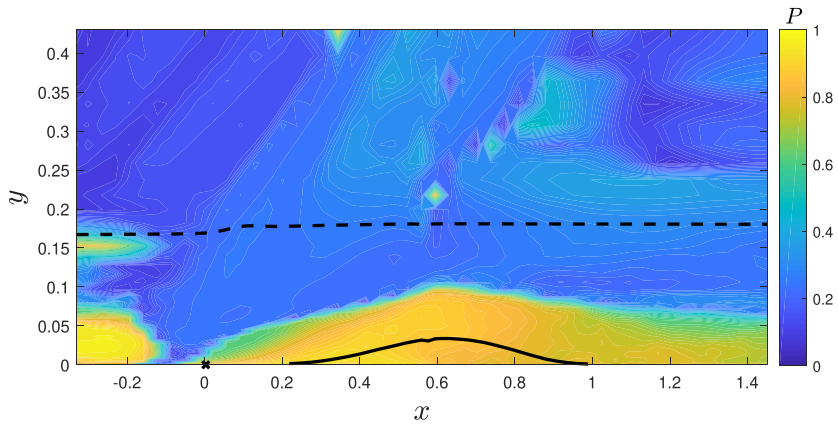
(b)$P-$paramter
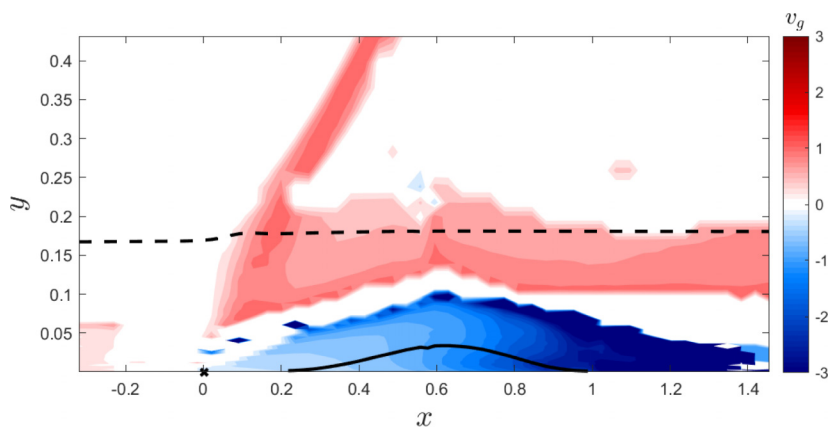
(c)Estimated group velocity

FIG. 7. Effect of the input position for prediction. Correlation values between predicted signal and LES data for the pressure fluctuations (a), P parameter for computing the causal relationship (b) and estimated group velocity (c). The solid line indicates the recirculation bubble and the dashed line indicates the boundary layer thickness. The cross indicates the considered output position.
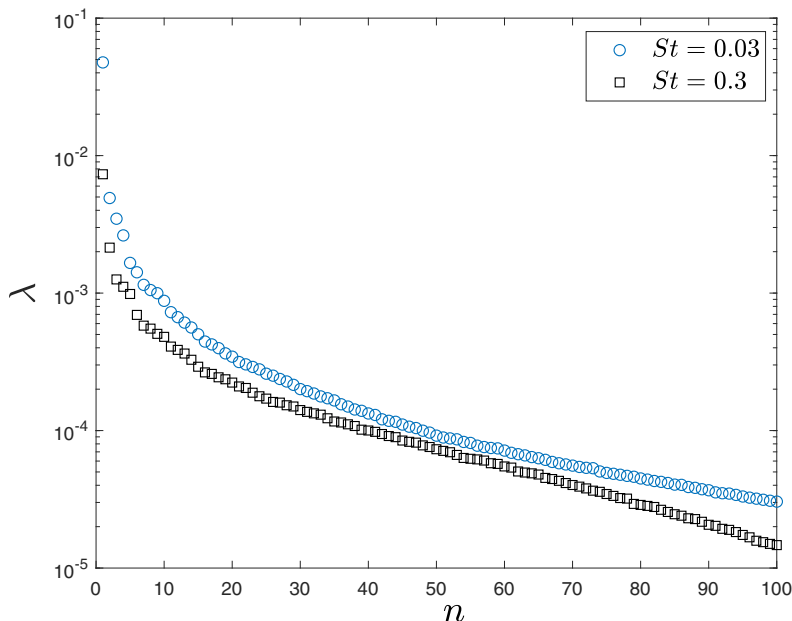
FIG. 8. Resulting SPOD eigenvalues computed for $St = 0.03$ (blue circles) and $St = 0.3$ (black squares).

a clear dominance of the first mode with respect to the other spectral modes. It is also noticeable that the low-frequency eigenvalues are higher over all the spectra. Hence, we consider only the first mode in the following analysis.

Figure 9 presents the structure of the streamwise velocity fluctuations of the first SPOD mode for the frequencies St = 0.03 and St = 0.3. The time evolution of the corresponding modes were obtained by multiplying the spectral mode by $e^{i2\pi ft}$. The resulting snapshots are reported in the movies in the Supplemental Material [51] for the time behavior of the SPOD modes at these two
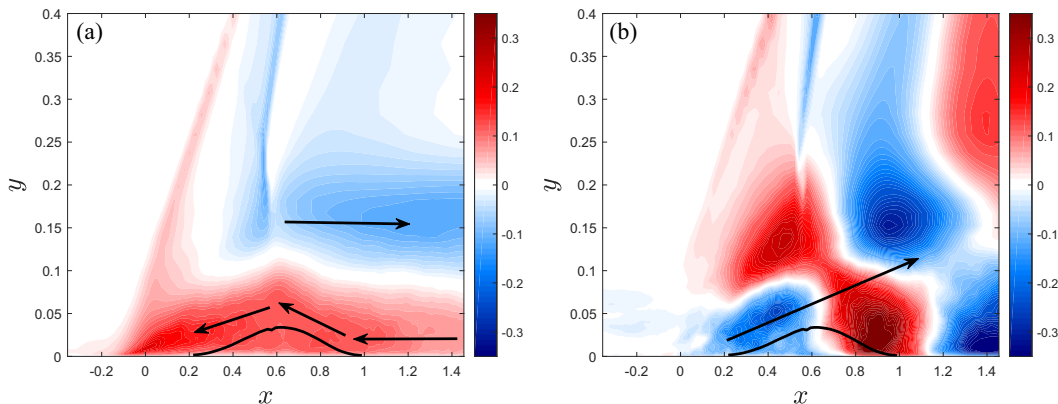

FIG. 9. Snapshot of the first SPOD mode of the streamwise velocity component at St = 0.03 (a) and St = 0.3 (b). The arrows depict schematically the motion of the streamwise velocity fluctuations. The contours correspond to the real part of the first SPOD mode. The time evolution of both modes is reported in the Supplemental Material [51].
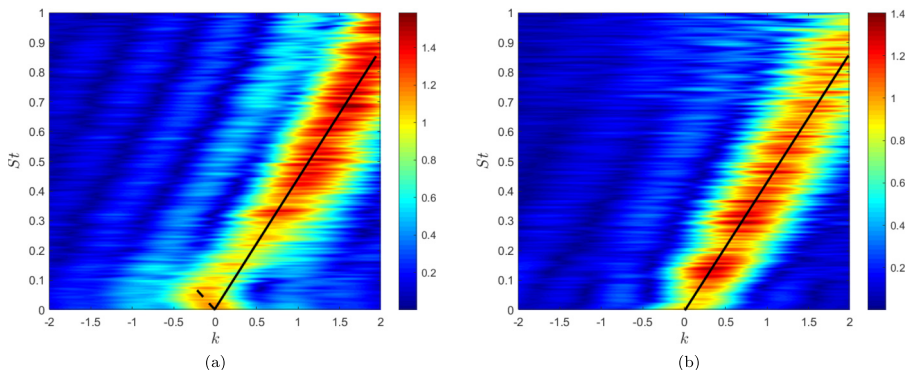
FIG. 10. Empirical dispersion relations, computed from the first SPOD mode of the streamwise velocity at $y = 0.05$ (a) and $y = 0.15$ (b). The logarithmic of the resulting power spectral density was taken. The solid vertical lines indicate constant group velocities estimated from the data. The dashed line in panel (a) presents the theoretical group velocity, computed from the linear stability analysis presented in Subsec. VI C.

frequencies. Interestingly, a wave propagating with negative phase velocity (from right to left) is observed for $St = 0.03$, on a position near the wall. Such motion surrounds the recirculation bubble toward the shock foot. At a higher wall-normal position ($y \approx 0.15$), there is a wave generated on the shock, propagating with positive group velocity (from left to right). The spatial footprint of this upstream traveling motion corresponds well to the causal locations presented in Fig. 7(b). This motion is schematized with the arrows in Fig. 9(a) and occurs for low-frequency modes in the vicinity of $St = 0.03$. For $St = 0.3$, only a wave traveling with positive phase velocity appears.

To shed further light on the dynamics of the upstream and downstream traveling waves, an empirical dispersion relation is calculated. This was obtained by computing the Fourier transform of the first SPOD mode (u) in the streamwise direction as a function of frequency St. A similar approach was employed to study acoustic resonances in turbulent jets [52]. The dispersion relation was computed for two wall-normal positions: $y = 0.05$, close to the wall but surrounding the recirculation bubble, and at $y = 0.15$. This procedure leads to the frequency wave-number power spectral density diagram of Fig. 10.

The phase velocity of the fluctuations at a given (St, k) pair is given by $v_p = 2\pi f / k$. Therefore, waves with negative values of k propagate upstream. Since the group velocity reads $v_g = 2\pi \, \partial f / \partial k$, we note that v_g changes between the two considered wall-normal locations. For the low frequencies ($St < 0.1$), there is a group of waves propagating upstream, with negative group velocity, and this only occurs in the near-wall region. On the other hand, at higher frequencies, the disturbances propagate with positive group velocity independently of the wall-normal position. The waves that travel with negative group velocity contribute to the causality relation between downstream areas and the shock motion, which was quantified by the correlations and the P parameter obtained from the transfer functions.

B. Reconstruction of the shock motion via SPOD

In this section, we evaluate how much of the shock oscillations can be recovered from a limited set of data, specifically selected from regions upstream or downstream of the approximate shock position. To quantify this analysis, we define the ratio

$$\frac{|u_{\mathrm{SPOD_{cut}}}|^2}{|u_{\mathrm{SPOD_{full}}}|^2} = \frac{\int_\Omega \sum_{i=1}^{N_b} (\lambda_{\mathrm{cut}_i} \psi_{\mathrm{cut}_i})^2 dx}{\int_\Omega \sum_{i=1}^{N_b} (\lambda_{\mathrm{full}_i} \psi_{\mathrm{full}_i})^2 dx}, \tag{12}$$
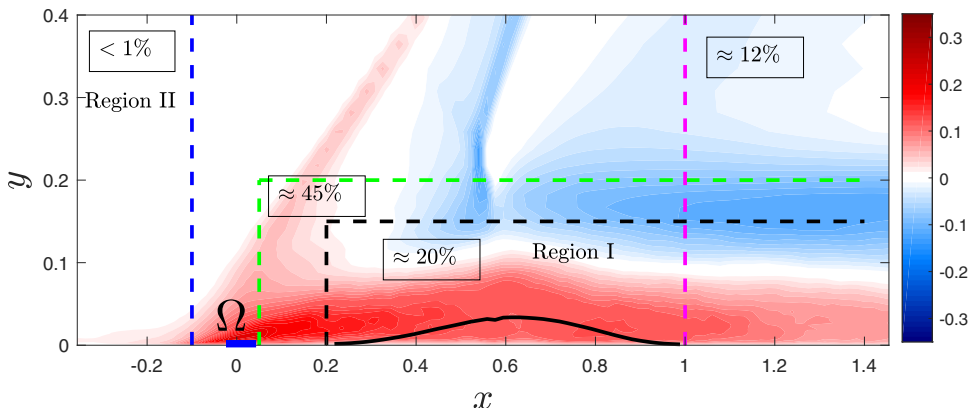
FIG. 11. First SPOD mode for the streamwise velocity at St $= 0.03$ and selected flow regions for the specific SPOD calculations. The portion of the energy at Ω which can be recovered in each case, in comparison to that of the full field, is highlighted in the corresponding rectangles.

where Ω is a horizontal line close to the wall encompassing the shock foot location, and the subscripts full and cut represent SPOD modes which were computed from the whole field and from a limited part of it using the weighting matrix $\mathbf{W}$, respectively. Equation (12) represents the ratio between the energy of the streamwise velocity fluctuations from SPOD modes computed using partial knowledge of the flow field and all the data available.

When the whole field is used in the computation, the weighting matrix $\mathbf{W}$ considers only the numerical quadrature corresponding to the use of a non-Cartesian coordinate system. To select specific flow regions, the numerical quadrature is multiplied by the matrix $\mathbf{W}_1$, where $\mathbf{W}_1 = 1$ for the selected region in the SPOD calculation, and $\mathbf{W}_1 = 0$ in the region excluded from the calculation. Therefore, the SPOD modes are computed considering only a portion of the field. In spite of this fact, the whole field can be reconstructed; areas which were not accounted in $\mathbf{W}_1$ but are observed in the SPOD modes can be related to fluctuations within the selected region where $\mathbf{W}_1 = 1$. This occurs due to the spatial coherence for the frequency where the SPOD mode is calculated. We attempt to evaluate through SPOD in regions that exclude the shock itself but are coherent with the shock motion. A similar approach was performed by Sano *et al.* [53] to reconstruct the acoustic field scattered by an airfoil from knowledge of its near field fluctuations.

Figure 11 provides distinct areas under evaluation. The energy is integrated over Ω, a straight line in the first grid position above the wall along $-0.05 < x < 0.05$. This line is shown in the plot. The spectral modes were calculated considering fluctuations within each of the rectangles limited by the dashed lines. For each region, $\mathbf{W}_1 = 1$ inside the rectangles and 0 outside them. Two rectangles are highlighted, indicating regions I and II, a rectangle downstream (black) and upstream (blue) of the shock, respectively. In the following, these two regions are considered in detail. The amount of energy that can be recovered is also shown in Fig. 11. It is clear that most of the energy of the shock fluctuations is related to downstream fluctuations. When considering the upstream region only, less than 1% of the energy is recovered.

The resulting eigenvalues of the SPOD modes at St $= 0.03$ are shown in Fig. 12 for regions I and II. The eigenvalues obtained from region I are close to the full data spectra and approximately three orders of magnitude higher than those computed from region II, upstream of the shock. The corresponding SPOD modes for each of these cases (not shown here for brevity) recover the shock motion, which is the most energetic structure for this frequency. Since the eigenvalues are related to the energy of the fluctuations, the results indicate that upstream fluctuations are weakly related to the shock motion. This agrees with the observations from Fig. 11. Therefore, the footprint of the low-frequency shock unsteadiness is significantly more related to downstream fluctuations.
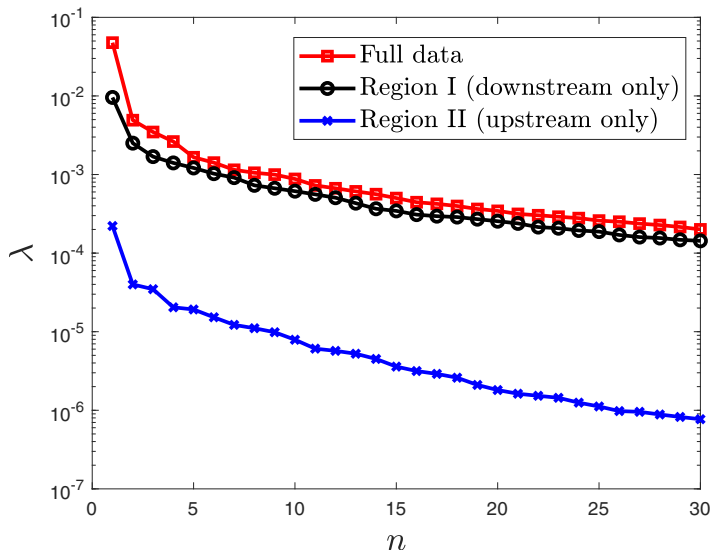
FIG. 12. Eigenvalues of the SPOD calculation obtained from the full field and regions I/II at St = 0.03.

C. Linear stability analysis of the mean turbulent flow

1. Formulation of the problem

In this section, the stability properties of the mean turbulent flow are presented. Our goal is to determine if the upstream traveling waves observed with the spectral mode decomposition can be predicted from the hydrodynamic stability theory. The underlying idea is that the optimal response of the flow, obtained with resolvent analysis, should be close to the leading SPOD mode if there exists a strong amplification mechanism. Here, we provide an evaluation of the presence of such a mechanism by studying the local linearized problem, considering a fixed streamwise location in the downstream region of the flow separation. The locally-parallel spatial stability problem [54,55] is evaluated such that the linearized compressible inviscid Navier–Stokes equations are cast in the form of

$$\mathcal{L}\hat{\hat{q}}(\alpha, \omega, y) = \alpha \mathcal{F}\hat{\hat{q}}(\alpha, \omega, y), \tag{13}$$

where the fluctuations $q = [u\, v\, T\, \rho]^T = \hat{\hat{q}}e^{[i(\alpha x - \omega t)]}$, where $\hat{\hat{q}} = [\hat{\hat{u}}\, \hat{\hat{v}}\, \hat{\hat{T}}\, \hat{\hat{\rho}}]^T$ is a vector of flow variables and the superscript T indicates a matrix transposition. The double hat indicates a double Fourier transform (from x to α and from t to ω). It should also be noted that only two-dimensional fluctuations (zero spanwise wave number) were considered, consistent with the previous analyses. The operators $\mathcal{L}$ and $\mathcal{F}$ are detailed in the Appendix.

The generalized eigenvalue problem of Eq. (A1) is solved for a given value ω. The boundary conditions considered are $\hat{v} = 0$ and $d\hat{T}/dy = 0$, at $y = 0$ and $y = \infty$. The equations are solved using the Chebyshev collocation method in the transverse direction [56], with the grid expanded from the interval of $[-1, 1]$ to $[0, H]$, where H is sufficiently large, using an algebraic mapping. The base flow consists of the turbulent mean at $x = 0.4$, which is about the middle of the recirculation region. In this position, upstream-traveling waves are visible in the leading SPOD mode.

The mean flow for the streamwise velocity component is fitted using a function appropriate for separated boundary layers [57],

$$\overline{U}(y) = \left[\frac{C_1}{4}U_1(y) + C_2\right]\tanh\left(\frac{y+1}{\delta_w}\right) \tag{14}$$
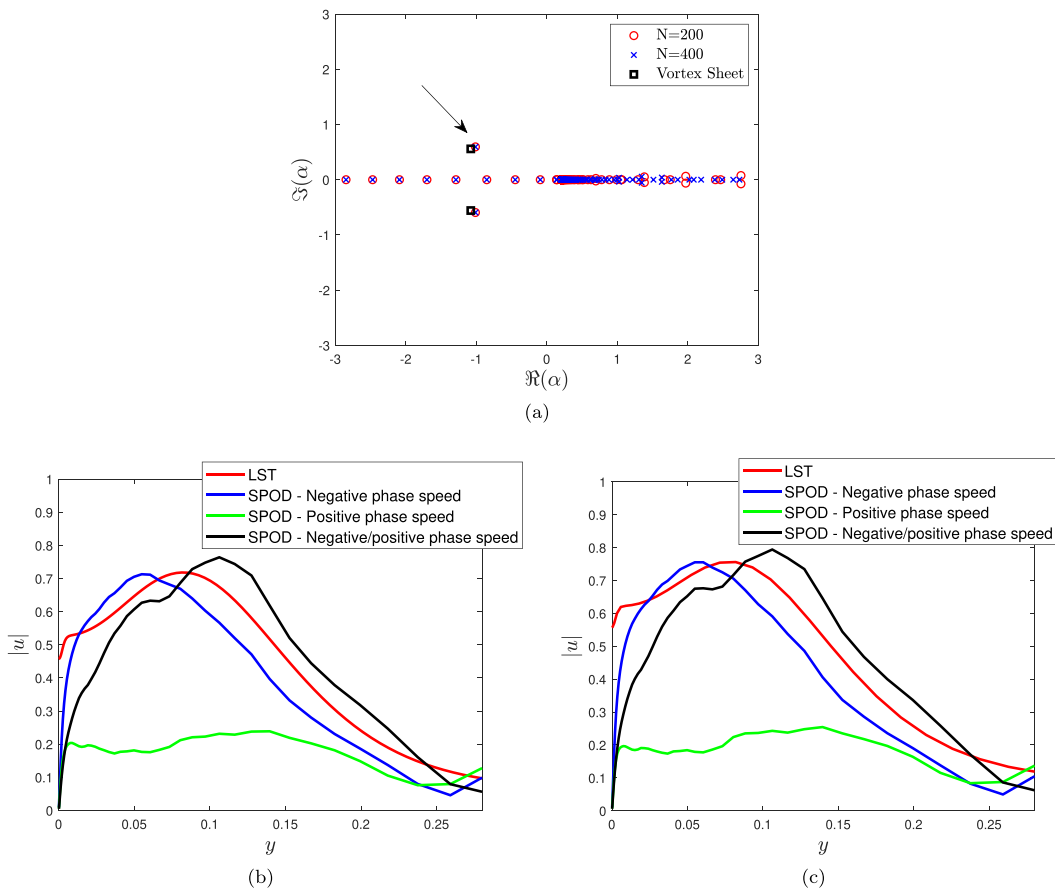
(a)

(b)

(c)

FIG. 13. Eigenspectrum at $St = 0.03$ and comparison between linear stability theory (red) and the first SPOD mode for the streamvise velocity (blue, green, black for $k < 0$, $k > 0$, no filter, respecitvely), for $St = 0.03$ and 0.06 at $x = 0.4$. The eigenspectrum was computed with two different discretizations, where N is the number of Chebyshev polynomials, in order to evaluate convergence, and compared to the vortex sheet results. The arrow highlights the unstable mode with negative phase velocity.

and

$$U_1(y) = \left[1 + \tanh\left(\frac{y - y_0}{a}\right)\right]\left[1 + \tanh\left(\frac{y - y_0}{b}\right)\right], \tag{15}$$

where C_1, C_2, a, b, and δ_w are found through a least-squares minimization for every streamwise profile evaluated. The mean temperature and density profiles have a weaker effect on the results and these are simply interpolated at the Chebyshev collocation points.

2. Linear stability results

A sample of the eigenspectrum computed via local linear stability theory (LST) for the Strouhal number $St = 0.03$ at $x = 0.4$ is shown in Fig. 13(a). Similar results were also observed at higher Strouhal numbers and multiple streamwise positions. The eigenspectrum shows a pair of discrete modes with negative phase speed. An analysis using Briggs' criterion, as detailed by Tam and Hu [60], shows that these modes have negative generalized velocity, and thus travel in the upstream direction. The discrete mode with $\text{Im}(\alpha) > 0$, highlighted in the figure, is thus an unstable mode

traveling upstream. Comparison of the eigenfunction against the first SPOD mode at the same location $x = 0.4$ is depicted in Figs. 13(b) and 13(c) for St = 0.03 and 0.06.

As discussed in Subsec. VI A, the leading low-frequency SPOD mode presents disturbances that propagate both downstream and upstream. In order to isolate the upstream and downstream components, a spatial filter was applied to the SPOD mode. This was performed by applying a a Fourier transform of the SPOD mode and retaining either the positive or negative values of k, for downstream or upstream traveling waves, respectively. This procedure is similar to the one employed in Ref. [58], and it is consistent with the negative phase speed of the LST mode. Although this method does not allow an exact splitting of the field into downstream and upstream traveling waves, since the lack of periodicity in x leads to errors in the Fourier transform, it nonetheless allows a separate quantitative assessment of these waves from the data set. This is possible for flows that develop slowly in x, such as jets [52,58].

For comparison purposes, the downstream/upstream components along with the full SPOD mode are shown. It is clear that the upstream part of the SPOD mode presents a compelling agreement with the LST prediction. The downstream and the full SPOD modes present a peak at regions farther from the wall. The downstream propagating component also presents a much lower amplitude, indicating that the upstream traveling wave contributes more to the total energy. The downstream traveling disturbances in the SPOD mode differ significantly from the upstream traveling stability mode. The group velocity of the unstable mode, computed using $v_g = \frac{d\omega}{d\alpha_r}$, where α_r indicates the real part of the spatial wave number, was observed to be $v_g = -0.45$ at St = 0.03. This value was overlaid to the empirical dispersion relation obtained from the SPOD modes presented in Fig. 10, resulting in a close agreement. Thus, both the eigenfunction and the eigenvalue obtained from the stability analysis match the leading SPOD mode.

The results indicate that the shock unsteadiness at the low-frequency range is related to upstream propagating fluctuations developing downstream of the separation point. This provides a physical mechanism for the influence of downstream regions on the shock motion, explaining the causal predictions obtained with the transfer functions in Sec. V, in accordance with the upstream traveling part of the dominant flow response obtained with the spectral mode decomposition. In what follows, we examine further properties of the unstable mode obtained from the stability analysis.

3. *Acoustic nature of the upstream traveling wave*

We now explore the nature of the unstable upstream traveling mode. It is known that compressibility effects lead to specific instability mechanisms that are absent from incompressible flows, as seen in boundary layers [59] and jets [60]. A recent work has explored the acoustic nature of discrete modes in jets, which are shown to behave similarly to acoustic duct modes [52]. The connection to duct acoustics was further developed by Martini *et al.* [61], showing that the unstable supersonic modes in jets found by Tam and Hu [60] are related to an acoustic mechanism, which renders such duct-like modes unstable. Here we explore the connection to acoustic modes by using the vortex-sheet model by Martini *et al.* [61].

The vortex sheet problem considers uniform flow above and below an infinitesimal vortex sheet, leading to an analytical dispersion relationship. The present recirculation region may be simplified as a vortex sheet such that

$$\text{Ma}(y < y_s) = -0.0350, \tag{16a}$$

$$\text{Ma}(y > y_s) = 2.0, \tag{16b}$$

where y_s is taken as the position where the velocity changes sign at $x = 0.4$. Considering $dp/dy = 0$ at $y = 0$ is equivalent to taking even modes in the model by Martini *et al.* [61], and thus the modes in the recirculation region are akin to even modes in compressible wakes. A solution for inviscid infinitesimal disturbances to the vortex sheet leads to the dispersion relationship, neglecting
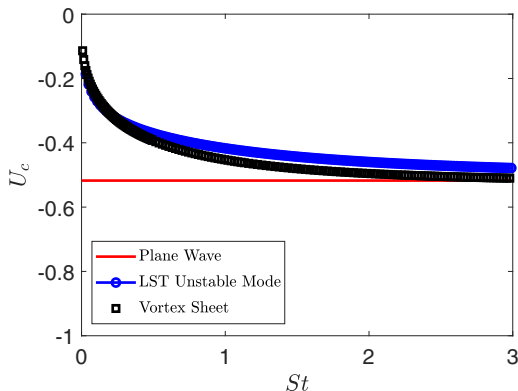
FIG. 14. Computed phase speed (U_c) of the unstable LST mode, vortex sheet, and plane-wave acoustic mode.

base-flow density variations

$$\tanh(\xi_{in}) = -\frac{\xi_{out}}{\xi_{in}}\left(\frac{U_{in} - c}{U_{out} - c}\right)^2,$$ (17)

where

$$\xi_{in,out} = \sqrt{\alpha^2[1 - (U_{in,out} - c)^2]}$$ (18)

with $U_{in} = \text{Ma}(y < y_s)/\text{Ma}_\infty$, $U_{out} = \text{Ma}(y > y_s)/\text{Ma}_\infty$ and $c = \omega/\alpha$, which corresponds to the phase speed of the corresponding vortex sheet mode, where the reference length is changed to y_s.

As discussed in Martini *et al.* [61], a number of discrete modes in the vortex sheet problem has acoustic nature and behaves similarly to duct modes. For a class of modes, the vortex sheet of a wake behaves similarly to a hard wall, and such acoustic modes may be thought of as slightly altered versions of duct modes. The analysis of the present upstream traveling unstable mode shows that it is related to the plane-wave duct mode, with wave fronts constant in x traveling upstream. Such acoustic modes can be obtained by finding the zeros of the dispersion relation, as outlined in Ref. [61], using a seeking algorithm which is started with a plane-wave mode as an initial guess. As shown in Fig. 13(a), the vortex-sheet result has an eigenvalue close to the solution of the Rayleigh equation, which indicates that the unstable mode obtained in the previous section may be approximated by the vortex-sheet model, as in the jet analysis by Towne *et al.* [52]. To demonstrate the correspondence between both instability modes (considering the LES velocity profile or the vortex sheet) and the plane-wave mode of duct acoustics, Fig. 14 shows the phase speed of the modes compared to the one of a plane wave propagating upstream, which is, with the present choice of nondimensional variables,

$$\overline{U} = u_{re} - c_0,$$ (19)

where u_{re} is the peak velocity at the recirculation and $c_0 = 1/\text{Ma}_\infty$ (the ambient sound speed nondimensionalized using the unperturbed velocity).

The results of Fig. 14 show a similar trend for the LST and vortex-sheet modes, showing that the vortex sheet approximates the behavior of the mode at hand. Furthermore, as the frequency increases, the phase speed approaches that of a plane wave, indicating that the upstream traveling wave could be related to a plane-wave acoustic mode which becomes unstable by its interaction with the sheared flow, as discussed by Martini *et al.* [61]. In the present linearized models, the upstream traveling mode remains unstable for rather large Strouhal numbers. However, the inclusion of viscosity could stabilize the mode at higher frequencies, and due to that reason it is not observed

in the higher frequency SPOD modes. As we deal with a turbulent flow, an eddy viscosity model may be appropriate [62–64]. Further work on this direction may help study why the upstream traveling mode only appears clearly at low Strouhal numbers.

VII. CONCLUSIONS

The dominant mechanisms driving the reflected shock unsteadiness were isolated using signal analysis and spectral mode decomposition of the flow fluctuation fields. First, we computed linear, single-input single-output transfer functions using pressure and streamwise velocity fluctuations to predict the unsteady shock fluctuations in a range of frequencies corresponding to the SBLI interaction determined via low-pass data filtering (St < 0.3). It was shown that locations downstream of the shock can accurately predict its fluctuations. Correlations of up to 0.6 were obtained between predicted and LES signals, even for the largest streamwise separation between input and output signals. The correlation magnitude strongly depends on data spanwise averaging, pointing to a predominantly 2D mechanism governing the shock unsteadiness.

Evaluation of the transfer functions in the frequency domain by means of a Hilbert transform suggests a causal relationship between flow regions downstream of the shock and its motion. When combined with the observed correlations, we conclude that the only causal inputs leading to high correlations with the shock are the locations surrounding and downstream of the recirculation bubble. In these regions, the fluctuations exhibit a negative phase velocity. These observations provide further evidence of the mechanisms suggested in previous investigations [13,16]. Causality was also detected between the upstream boundary layer and the shock motion, as reported by Ganapathisubramani *et al.* [50], but with a much lower correlation when compared to downstream locations. This is possibly related to the absence of large-scale structures within the boundary layer in the current numerical database.

This evaluation was complemented by the computation of the spectral modes from the SPOD analysis which pointed to the existence of an upstream traveling wave in the leading mode at St = 0.03. The Fourier transform of the leading mode confirmed the negative group velocity for frequencies up to St ≈ 0.1 in the near-wall region. On the other hand, the same mode presented a positive group velocity at higher wall-normal positions. In addition, we demonstrated that a significant portion of the energy of the shock motion can be recovered from a limited set of measurements taken downstream of the shock. Comparison of the corresponding eigenvalues indicated that the downstream region contributes more significantly to the shock unsteadiness than the upstream region.

Finally, a linear stability analysis was performed using the mean turbulent flow. The LST evaluation indicates the presence of an unstable upstream traveling mode. A close match was observed between LST and the upstream traveling part of the SPOD mode both in terms of the shape of the predicted fluctuations and their resulting phase speed. An analogy of these results with a vortex sheet model indicated that such an unstable mode is of acoustic nature, corresponding to an acoustic plane wave propagating upstream, which becomes unstable due to its interaction with the shear layer. Such acoustic mode provides the mechanism by which downstream fluctuations propagate upstream and lead to shock wave oscillations. The identification of such mechanisms points to interesting directions, as the manipulation of the acoustic mode by wall treatment may lead to attenuation of undesirable shock unsteadiness.

APPENDIX: OPERATORS FOR THE LINEAR STABILITY ANALYSIS

We follow Ref. [55] for the spatial linear stability analysis. The compressible inviscid Navier-Stokes equations are linearized over the mean flow, with the quantities decomposed into a mean plus time-dependent fluctuation. Application of the ansatz $q(\alpha, \omega, y) = [u(\alpha, \omega, y)\, v(\alpha, \omega, y)\, T(\alpha, \omega, y)\, \rho(\alpha, \omega, y)]^T = \hat{q}(\alpha, \omega, y)e^{[i(\alpha x - \omega t)]}$ in the linearized equations, with $u(\alpha, \omega, y)$, $v(\alpha, \omega, y)$, $T(\alpha, \omega, y)$, and $\rho(\alpha, \omega, y)$ being the fluctuating stream/wall-normal velocities, temperature, and density, leads to a generalized eigenvalue problem,

$$\mathcal{L}\hat{q}(\alpha, \omega, y) = \alpha \mathcal{F}\hat{q}(\alpha, \omega, y). \tag{A1}$$

The operators $\mathcal{L}$ and $\mathcal{F}$, for the compressible inviscid case of an ideal gas, are given as

$$\mathcal{L} = \begin{pmatrix} -i\overline{\rho}\omega & \overline{\rho}\frac{\partial \overline{U}}{\partial y} & 0 & 0 \\ 0 & -i\overline{\rho}\omega & \frac{1}{\gamma \mathrm{Ma}_\infty^2}\frac{\partial \overline{\rho}}{\partial y} + \frac{1}{\gamma \mathrm{Ma}_\infty^2}\overline{\rho}\frac{\partial}{\partial y} & \frac{1}{\gamma \mathrm{Ma}_\infty^2}\frac{\partial \overline{T}}{\partial y} + \frac{1}{\gamma \mathrm{Ma}_\infty^2}\overline{T}\frac{\partial}{\partial y} \\ 0 & \overline{\rho}\frac{\partial \overline{T}}{\partial y} + (\gamma - 1)\frac{\partial}{\partial y} & -i\omega\overline{\rho} & 0 \\ 0 & \frac{\partial \overline{\rho}}{\partial y} + \overline{\rho}\frac{\partial}{\partial y} & 0 & -i\omega \end{pmatrix}, \tag{A2}$$

$$\mathcal{F} = \begin{pmatrix} -i\overline{\rho}\,\overline{U} & 0 & -i\frac{1}{\gamma \mathrm{Ma}_\infty^2}\overline{\rho} & -i\frac{1}{\gamma \mathrm{Ma}_\infty^2}\overline{T} \\ 0 & -i\overline{\rho}\,\overline{U} & 0 & 0 \\ -i(\gamma - 1) & 0 & -i\overline{\rho}\,\overline{U} & 0 \\ -i\overline{\rho} & 0 & 0 & -i\overline{U} \end{pmatrix}, \tag{A3}$$

where the overbar indicates mean quantities and $\gamma = 1.4$. Solution of Eq. (A1) is made by imposing a given value of ω and computing the corresponding α (eigenvalue) and $\hat{q}$ (eigenmode). The results of the linear stability code, written in primitive variables, have been compared to those of the method used in Ref. [65], with similar results, which validates the current implementation.

[1] Y. Andreopoulos, J. H. Agui, and G. Briassulis, Shock wave-turbulence interactions, Annu. Rev. Fluid Mech. **32**, 309 (2000).

[2] H. Babinsky and J. K. Harvey, *Shock Wave-Boundary-Layer Interactions*, Vol 32 (Cambridge University Press, Cambridge, UK, 2011).

[3] N. T. Clemens and V. Narayanaswamy, Low-frequency unsteadiness of shock wave/turbulent boundary layer interactions, Annu. Rev. Fluid Mech. **46**, 469 (2014).

[4] J. M. Delery, Shock wave/turbulent boundary layer interaction and its control, Prog. Aerospace Sci. **22**, 209 (1985).

[5] D. S. Dolling, Fifty years of shock-wave/boundary-layer interaction research: What next? AIAA J. **39**, 1517 (2001).

[6] J. P. Dussauge, P. Dupont, and J. F. Debiève, Unsteadiness in shock wave boundary layer interactions with separation, Aerosp. Sci. Technol. **10**, 85 (2006).

[7] D. V. Gaitonde, Progress in shock wave/boundary layer interactions, Prog. Aerospace Sci. **72**, 80 (2015).

[8] S. J. Beresh, N. T. Clemens, and D. S. Dolling, Relationship between upstream turbulent boundary-layer velocity fluctuations and separation shock unsteadiness, AIAA J. **40**, 2412 (2002).

[9] L. Brusniak and D. S. Dolling, Physics of unsteady blunt-fin-induced shock wave/turbulent boundary layer interactions, J. Fluid Mech. **273**, 375 (1994).

[10] K. J. Plotkin, Shock wave oscillation driven by turbulent boundary-layer fluctuations, AIAA J. **13**, 1036 (1975).

[11] B. Ganapathisubramani, N. T. Clemens, and D. S. Dolling, Low-frequency dynamics of shock-induced separation in a compression ramp interaction, J. Fluid Mech. **636**, 397 (2009).

[12] R. A. Humble, G. E. Elsinga, F. Scarano, and B. W. Van Oudheusden, Three-dimensional instantaneous structure of a shock wave/turbulent boundary layer interaction, J. Fluid Mech. **622**, 33 (2009).

[13] E. Touber and N. D. Sandham, Large-eddy simulation of low-frequency unsteadiness in a turbulent shock-induced separation bubble, Theor. Comput. Fluid Dyn. **23**, 79 (2009).

[14] P. Dupont, C. Haddad, and J. F. Debieve, Space and time organization in a shock-induced separated boundary layer, J. Fluid Mech. **559**, 255 (2006).

[15] M. Wu and M. P. Martin, Analysis of shock motion in shockwave and turbulent boundary layer interaction using direct numerical simulation data, J. Fluid Mech. **594**, 71 (2008).

[16] S. Piponniau, J. P. Dussauge, J. F. Debieve, and P. Dupont, A simple model for low-frequency unsteadiness in shock-induced separation, J. Fluid Mech. **629**, 87 (2009).

[17] L. Larchevêque, Low- and Medium-Frequency Unsteadinesses in a Transitional Shock–Boundary Reflection with Separation, in *54th AIAA Aerospace Sciences Meeting* (AIAA, 2016), p. 1833.

[18] A. Sansica, N. D. Sandham, and Z. Hu, Instability and low-frequency unsteadiness in a shock-induced laminar separation bubble, J. Fluid Mech. **798**, 5 (2016).

[19] S. Priebe and M. P. Martín, Low-frequency unsteadiness in shock wave–turbulent boundary layer interaction, J. Fluid Mech. **699**, 1 (2012).

[20] S. Priebe, J. H. Tu, C. W. Rowley, and M. P. Martín, Low-frequency dynamics in a shock-induced separated flow, J. Fluid Mech. **807**, 441 (2016).

[21] V. Pasquariello, S. Hickel, and N. A. Adams, Unsteady effects of strong shock-wave/boundary-layer interaction at high Reynolds number, J. Fluid Mech. **823**, 617 (2017).

[22] J. W. Nichols, J. Larsson, M. Bernardini, and S. Pirozzoli, Stability and modal analysis of shock/boundary layer interactions, Theor. Comput. Fluid Dyn. **31**, 33 (2016).

[23] T. Jiang, A. M. Schreyer, L. Larchevêque, S. Piponniau, and P. Dupont, Velocity spectrum estimation in shock-wave/turbulent boundary-layer interaction, AIAA J. **55**, 3486 (2017).

[24] S. Pirozzoli and F. Grasso, Direct numerical simulation of impinging shock wave/turbulent boundary layer interaction at $m = 2.25$, Phys. Fluids **18**, 065113 (2006).

[25] K. Sasaki, S. Piantanida, A. V. G. Cavalieri, and P. Jordan, Real-time modelling of wave packets in turbulent jets, J. Fluid Mech. **821**, 458 (2017).

[26] K. Sasaki, R. Vinuesa, A. V. G. Cavalieri, P. Schlatter, and D. S. Henningson, Transfer functions for flow predictions in wall-bounded turbulence, J. Fluid Mech. **864**, 708 (2019).

[27] C. Picard and J. Delville, Pressure velocity coupling in a subsonic round jet, Int. J. Heat Fluid Flow **21**, 359 (2000).

[28] A. Towne, O. T. Schmidt, and T. Colonius, Spectral proper orthogonal decomposition and its relationship to dynamic mode decomposition and resolvent analysis, J. Fluid Mech. **847**, 821 (2018).

[29] A. V. G. Cavalieri, P. Jordan, and L. Lesshafft, Wave-packet models for jet dynamics and sound radiation, Appl. Mech. Rev. **71**, 020802 (2019).

[30] P. Morra, P. A. S. Nogueira, A. V. G. Cavalieri, and D. S. Henningson, The colour of forcing statistics in resolvent analyses of turbulent channel flows, J. Fluid Mech. **907**, A24 (2021).

[31] A. Zare, M. R. Jovanović, and T. T. Georgiou, Colour of turbulence, J. Fluid Mech. **812**, 636 (2017).

[32] A. M. Schreyer, J. J. Lasserre, and P. Dupont, Development of a dual-PIV system for high-speed flow applications, Exp. Fluids **56**, 187 (2015).

[33] F. Ducros, V. Ferrand, F. Nicoud, C. Weber, D. Darracq, C. Gacherieu, and T. Poinsot, Large-eddy simulation of the shock/turbulence interaction, J. Comput. Phys. **152**, 517 (1999).

[34] P. L Roe, Approximate Riemann solvers, parameter vectors, and difference schemes, J. Comput. Phys. **43**, 357 (1981).

[35] L. Agostini, L. Larchevêque, and P. Dupont, Mechanism of shock unsteadiness in separated shock/boundary-layer interactions, Phys. Fluids **27**, 126103 (2015).

[36] E. Garnier, P. Sagaut, and M. Deville, Large eddy simulation of shock/boundary-layer interaction, AIAA J. **40**, 1935 (2002).

[37] N. Jarrin, S. Benhamadouche, D. Laurence, and R. Prosser, A synthetic-eddy-method for generating inflow conditions for large-eddy simulations, Int. J. Heat Fluid Flow **27**, 585 (2006).

[38] L. Agostini, L. Larchevêque, P. Dupont, J. F. Debiève, and J. P. Dussauge, Zones of influence and shock motion in a shock/boundary-layer interaction, AIAA J. **50**, 1377 (2012).

[39] A. M. Schreyer, L. Larchevêque, and P. Dupont, Method for spectra estimation from high-speed experimental data, AIAA J. **54**, 557 (2016).

[40] E. Touber and N. D. Sandham, Low-order stochastic modelling of low-frequency motions in reflected shock-wave/boundary-layer interactions, J. Fluid Mech. **671**, 417 (2011).

[41] M. S. Loginov, N. A. Adams, and A. A. Zheltovodov, Large-eddy simulation of shock-wave/turbulent-boundary-layer interaction, J. Fluid Mech. **565**, 135 (2006).

[42] J. S. Bendat and A. G. Piersol, *Random Data: Analysis and Measurement Procedures*, Wiley Series in Probability and Statistics (John Wiley & Sons, New York, 2011), Vol. 729.

[43] G. T. Rocklin, J. Crowley, and H. Vold, A comparison of h_1, h_2, and h_v frequency response functions, in *Proceedings of the Third International Modal Analysis Conference* (International Operational Modal Analysis Conference, Spain, 1985), Vol. 1, pp. 272–278.

[44] J. S. Bendat, Spectral techniques for nonlinear system analysis and identification, Shock Vibrat. **1**, 21 (1993).

[45] W. H. Press, *Numerical Recipes: The Art of Scientific Computing*, 3rd ed. (Cambridge University Press, Cambridge, UK, 2007).

[46] K. Sasaki, G. Tissot, A. V. G. Cavalieri, F. J. Silvestre, P. Jordan, and D. Biau, Closed-loop control of a free shear flow: A framework using the parabolized stability equations, Theor. Comput. Fluid Dyn. **32**, 765 (2018).

[47] A. V. G. Cavalieri, D. Rodríguez, P. Jordan, T. Colonius, and Y. Gervais, Wave packets in the velocity field of turbulent jets, J. Fluid Mech. **730**, 559 (2013).

[48] K. Sasaki, P. Morra, A. V. G. Cavalieri, A. Hanifi, and D. S. Henningson, On the role of actuation for the control of streaky structures in boundary layers, J. Fluid Mech. **883**, A34 (2020).

[49] O. Semeraro, V. Jaunet, P. Jordan, A. V. Cavalieri, and L. Lesshafft, Stochastic and harmonic optimal forcing in subsonic jets, in *22nd AIAA/CEAS Aeroacoustics Conference* (AIAA, 2016), p. 2935.

[50] B. Ganapathisubramani, N. T. Clemens, and D. S. Dolling, Effects of upstream boundary layer on the unsteadiness of shock-induced separation, J. Fluid Mech. **585**, 369 (2007).

[51] See Supplemental Material at http://link.aps.org/supplemental/10.1103/PhysRevFluids.6.064609 for the time-domain behaviour of the dominant SPOD modes for $St = 0.03$ and $St = 0.3$.

[52] A. Towne, A. V. G. Cavalieri, P. Jordan, T. Colonius, O. Schmidt, V. Jaunet, and G. A. Brès, Acoustic resonance in the potential core of subsonic jets, J. Fluid Mech. **825**, 1113 (2017).

[53] A. Sano, L. I. Abreu, A. V. G. Cavalieri, and W. R. Wolf, Trailing-edge noise from the scattering of spanwise-coherent structures, Phys. Rev. Fluids **4**, 094602 (2019).

[54] A. Hanifi, P. J. Schmid, and D. S. Henningson, Transient growth in compressible boundary layer flow, Phys. Fluids **8**, 826 (1996).

[55] M. R. Malik, S. Chuang, and M. Y. Hussaini, Accurate numerical solution of compressible, linear stability equations, Zeitschr. Angew. Math. Phys. ZAMP **33**, 189 (1982).

[56] L. N. Trefethen, *Spectral Methods in MATLAB* (Society for Industrial Mathematics, Philadelphia, 2000), Vol. 10.

[57] P. C. Ormonde, A. V. G. Cavalieri, R. G. A. da Silva, and A. C. Avelar, Passive control of coherent structures in a modified backwards-facing step flow, Exp. Fluids **59**, 1 (2018).

[58] D. Edgington-Mitchell, V. Jaunet, P. Jordan, A. Towne, J. Soria, and D. Honnery, Upstream-travelling acoustic jet modes as a closure mechanism for screech, J. Fluid Mech. **855**, R1 (2018).

[59] L. M. Mack, Linear stability theory and the problem of supersonic boundary-layer transition, AIAA J. **13**, 278 (1975).

[60] C. K. W. Tam and F. Q. Hu, On the three families of instability waves of high-speed jets, J. Fluid Mech. **201**, 447 (1989).

[61] E. Martini, A. Cavalieri, and P. Jordan, Acoustic modes in jet and wake stability, J. Fluid Mech. **867**, 804 (2019).

[62] J. C. Del Alamo and J. Jimenez, Linear energy amplification in turbulent channels, J. Fluid Mech. **559**, 205 (2006).

[63] Y. Hwang and C. Cossu, Linear non-normal energy amplification of harmonic and stochastic forcing in turbulent channel flow, J. Fluid Mech. **664**, 51 (2010).

[64] P. Morra, O. Semeraro, D. S. Henningson, and C. Cossu, On the relevance of Reynolds stresses in resolvent analyses of turbulent wall-bounded flows, J. Fluid Mech. **867**, 969 (2019).

[65] W. R. Wolf, A. V. G. Cavalieri, B. Backes, E. Morsch-Flho, and J. L. F. Azevedo, Sound and sources of sound in a model problem with wake interaction, AIAA J. **53**, 2588 (2015).